ARTICLE

Received 00th January 20xx,
Accepted 00th January 20xx

DOI: 10.1039/x0xx00000x

Wet-etching Fabrication of Flexible and Transparent Silicon Frameworks for Imperceptible Wearable Electronics

Tingyu Wei,‡[a] Yihao Shi,‡[a] Bingchang Zhang,*[b] Yu Ding,[c] Jiahao Qin,[ade] Xinyue Hu,[a] Jia Yu,[a] Ruiyuan Liu*[c] and Xiaohong Zhang*[a]

Electronic materials with mechanical flexibility and visual transparency are highly desirable for imperceptible wearable electronics that can alleviate wearing reluctance. However, as a well-functioned material in modern electronics, silicon is usually rigid and opaque. Here, a novel strategy is proposed to fabricate single-crystalline silicon frameworks (sc-SiFs) through alkali etching. The as-prepared sc-SiFs exhibit a minimum bending radius of 6 mm and a light transmittance of up to 77%. The remarkable performance results from the unique framework structures, which provide adequate space for stress relief and light transmission. By precisely controlling the structural parameters, the mechanical and optical properties of SiFs can be easily tailored to meet the diverse requirements of various applications. Despite new properties, sc-SiFs preserve the electronic properties of silicon, which makes them good candidates for wearable electronics. As an example, imperceptible bending sensors based on sc-SiFs have been constructed to detect physiological activities, including facial expressions and swallow. This work provides a scalable method for fabricating flexible and transparent silicon materials, which will facilitate the development of imperceptible wearable electronics.

Introduction

Wearable electronics have attracted intensive attention due to their potential applications in healthcare, man-machine interaction, and bionic robots.[1–5] For instance, electronic skin is able to detect human activities across a wide range of limb movements in real time.[6] Electronic patches can be fixed for tracking vital signs of premature infants.[7] And bionic skins can reproduce skin functions such as touch, pain, and temperature perception.[8] In these application scenarios, flexible and transparent electronic devices with mechanical and visual imperceptibility are very desired. Mechanical imperceptibility means that the device has good flexibility and can conformally contact with skins without a sense of restraint, which benefits precise extraction of bio-signals and ensures wearing comfort.[9,10] Visual imperceptibility refers to the high transparency of the device, making it inconspicuous to others, ensuring aesthetics and privacy in wearable applications. In addition, visual information can penetrate the transparent device and be utilized for comprehensive clinical diagnosis.[11]

In order to obtain imperceptible devices, the applied electronic materials need to be flexible and transparent. Extensive research has been conducted to develop flexible and transparent electronic materials, such as transparent conducting oxides,[12–14] metal nanowires (silver and copper nanowires),[15–17] organic semiconductors,[18–20] and perovskites.[21,22] Although they can be used to fabricate flexible and transparent solar cells,[23] transparent energy storage devices,[24–26] transparent soft robot,[27,28] transparent heater,[29] transparent air filter,[30,31] touch screens,[32] displays,[33] photodetectors,[34] and other devices,[35,36] the challenges of low carrier mobility and poor stability still persist in these material systems.[37,38] In contrast, silicon, as the core active material in traditional electronics, exhibits excellent electrical properties and stability, but is rigid and opaque, hardly meeting the material requirements of the booming imperceptible electronics.[39,40]

To solve the above problems, our group recently developed novel flexible and transparent single-crystalline Si frameworks (sc-SiFs) by setting up holes in thinned silicon wafers with

[a.] Institute of Functional Nano & Soft Materials (FUNSOM), Jiangsu Key Laboratory for Carbon-Based Functional Materials and Devices, Soochow University, Suzhou, Jiangsu 215123, P. R. China. Email: xiaohong_zhang@suda.edu.cn
[b.] School of Optoelectronic Science and Engineering, Key Laboratory of Advanced Optical Manufacturing Technologies of Jiangsu Province, Key Laboratory of Modern Optical Technologies of Education Ministry of China, Soochow University, Suzhou, Jiangsu 215123, P. R. China. Email: zhangbingchang@suda.edu.cn
[c.] College of Energy, Soochow Institute of Energy and Material Innovations, Key Laboratory for Advanced Carbon Materials and Wearable Energy Technologies of Jiangsu Province, Soochow University, Suzhou, Jiangsu 215123, P. R. China. Email: ryliu@suda.edu.cn
[d.] Department of Materials Science and Engineering, Monash University, Clayton, VIC 3800, Australia.
[e.] Suzhou Industrial Park Monash Research Institute of Science and Technology, Monash University, Suzhou, Jiangsu 215123, P. R. China.

†Electronic Supplementary Information (ESI) available: [Photographs of stainless-steel fixtures with a silicon wafer fixed in the middle, photographs of a single-thinned silicon wafer and SEM images of sc-SiFs obtained by reactive ion etching (RIE) and wet etching]. See DOI: 10.1039/x0xx00000x

‡ Tingyu Wei and Yihao Shi contributed equally to this work.

masked deep silicon etching. The holes provide a space for stress relief, which reduces strain concentration and allows the frameworks to withstand large bending deformation without mechanical fracture.[41] On the other hand, the holes allow the penetration of light, which makes the sc-SiFs transparent. Besides the new features of flexibility and transparency, the sc-SiFs maintain the electronic property of Si materials and are compatible with Si-based device process. This endows the capability of fabricating high-performance Si-based flexible transparent devices. For example, efficient and transparent solar cells based on sc-SiFs with a transparency of 20% and energy conversion efficiency of up to 14.5% have been reported.[42–44] Our group has prepared high-performance sc-SiF-based flexible and transparent photodetectors, which exhibit a record response speed, high responsivity, and high specific detectivity.[41] Despite these progresses, the reported sc-SiFs were fabricated through dry etching, which askes specialized and expensive equipment, and the etching area is limited in one experiment. Moreover, it causes damage and ion contamination on the side walls of sc-SiFs, which will harm the device performance.[45] These problems hinder the extensive research and application of sc-SiFs. Besides, while wet etching is a common method for silicon etching, it remains unclear whether and how sc-SiFs can be manufactured through wet etching. Some issues such as the masking method for wet etching, the single-side etching of silicon wafers, as well as the morphology and structure control, need to be addressed.

In this work, a scalable method for fabricating flexible and transparent sc-SiFs is developed by combining lithography and highly efficient wet etching technology. Through the design of appropriate experimental setups and procedures, controlled fabrication of sc-SiFs was achieved and the impact of experimental conditions on sc-SiFs morphology was revealed. The as-prepared sc-SiFs exhibit a minimum bending radius of 6 mm, and a light transmittance of up to 77%. By controlling the structural parameters, the flexibility and transparency of the SiFs can be tailored to meet the requirements of various applications. Moreover, the research demonstrates the potential of these flexible and transparent sc-SiFs in imperceptible wearable electronics by taking wearable bending sensors as an example. The sensors are capable of detecting physiological activities, including facial expressions and swallow, which is significant for healthcare and human-machine interaction. This work provides a new strategy to fabricate flexible and transparent silicon materials, which will promote the research and application of silicon-based imperceptible wearable electronics.

Results and discussion

The wet-etching fabrication of flexible and transparent sc-SiFs is divided into two steps including thinning the wafer and alkali etching with patterned silica as the mask. 200 µm-thick, double-side-polished and oxidized N-type <100> silicon wafers are adopted to fabricate sc-SiFs. Before thinning the wafer, a

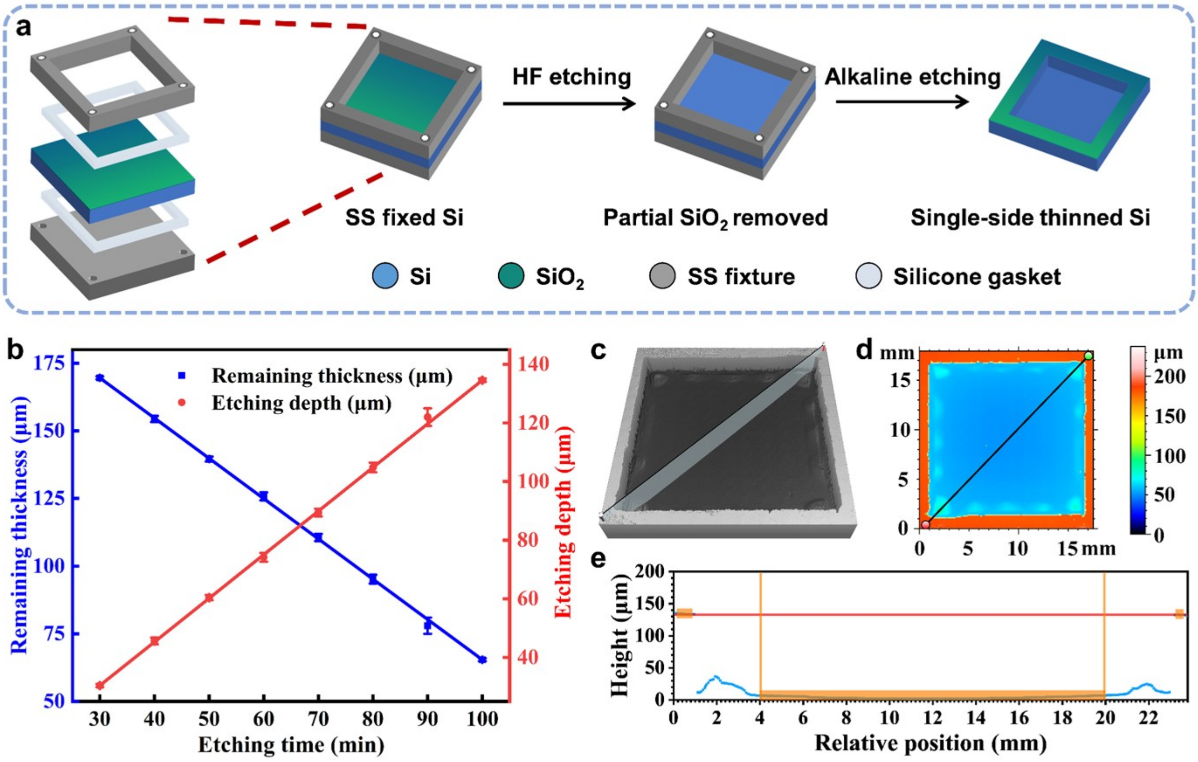

Fig. 1 Single-sided thinning of the silicon wafer. (a) Flowchart of thinning. (b) Etching rate in 50 % KOH solution at 95 °C. (c) 3D morphology, (d) depth map, and (e) step height of the thinned silicon wafer.

photolithography process for patterning silica is first conducted because thinned silicon wafers are fragile in photolithography manipulation. For thinning silicon wafers, a stainless-steel (SS) fixture and silicone gaskets were used to protect the photoresist pattern on one side and make thinning only occur on the other side (Fig. 1(a)). After fixing the silicon wafer with the fixture, the oxide layer on the exposed surface was removed with 40% HF. The wafer was then etched in 50% KOH solution, which was heated to 95 °C in a water bath. The thickness of the sample at different etching time was measured and plotted for accurately controlling the thickness (Fig. 1(b)). The remaining thickness of the sample has a linear relationship with the etching time. According to the relationship between single-side etching depth and time, the etching rate was fitted as 1.5 μm min^{-1}. The results show that the etching rate in our experiment is constant, and the thickness of the thinned sample can be effectively controlled with etching time. Notably, the etching rate increases with the increase of reaction temperature. For example, the etching rate is 0.5 μm min^{-1} at 70 °C, and 1.5 μm min^{-1} at 95 °C. It is beneficial to accelerate the reaction rate and reduce the reaction time by adopting the water bath temperature of 95 °C. Furthermore, the morphology and uniformity of the thinned silicon wafer were investigated with three-dimensional (3D) laser confocal microscopy. As shown in Fig. 1(c), the sealing area was effectively protected from etching by using the fixture and a 16 mm × 16 mm square pit was formed due to the etching of silicon wafer. The depth map shows that the height of the etched surface is uniform in the middle zone of approximately 14 mm × 14 mm, while the height fluctuates at the edge zone due to bubbling and the edge effect (Fig. 1(d)).[46] The height fluctuating can be explained as follows. When silicon reacts with alkali, hydrogen is produced (equation (1)) and gathers at the edge of the fixture, forming bubbles (Fig. S4, ESI†). The production and movement of bubbles will affect the etching and lead to the height fluences at the edge zone.

$$Si + 2KOH + H_2O = K_2SiO_3 + 2H_2\uparrow \quad (1)$$

The height-position curve along the diagonal line of the square pit further confirms the uniformity of the thinned silicon wafer in the middle zone (Fig. 1(e)). Furthermore, a piece of 4-inch wafer was etched in the same way (Fig. S5, ESI†). The silicon wafer has a exposed circular zone with the diameter of 7 cm. After alkali etching, it is found that the height in the middle circular zone with the diameter of 6.4 cm is uniform and the non-uniformity in height only occurs within 0.3 cm from the edge, which is similar to the size of non-uniform zones at the edges of 16 mm × 16 mm samples. The edge effect has limited impact on the overall thinning. The results indicates that this method allows for the acquisition of large-area and uniform thinned silicon wafers.

After obtaining thinned silicon wafers, the next step is alkali etching with patterned silica as the mask (Fig. 2(a)). The thinned silicon wafer is treated in a buffered oxide etchant (BOE) solution. With patterned photoresist as the mask (Fig. 2(b)), the exposed oxide layer was removed and silicon under them was exposed (Fig. 2(c)). Then, the photoresist on the silicon wafer was dissolved in acetone. The retained silicon oxide layer replicates the pattern of the photoresist (Fig. 2(d)). The retained silicon oxide pattern serves as the mask in the next step of wet etching. With the patterned oxide layer as the mask, the sample was etched again in 50% KOH solution at 95 °C. The etching rate of silicon dioxide in KOH is much slower (1-2 orders of magnitude) than that of silicon.[47] Therefore, the oxide layer protected the silicon under them from being etched. In contrast, exposed silicon was etched and gradually hollowed out (Fig. 2(e)), and sc-SiFs were obtained. It is noted that the thickness of the thinned silicon wafer needs to be at least twice the thickness of the target sc-SiFs due to the simultaneous etching on both sides in this step. The final thickness of sc-SiFs is determined by the thickness of the thinned silicon wafer and the time of the second-step etching. Though thinner sc-SiFs have better flexibility and higher light transmittance, sc-SiFs with the thickness less than 10 μm are easy to fracture when

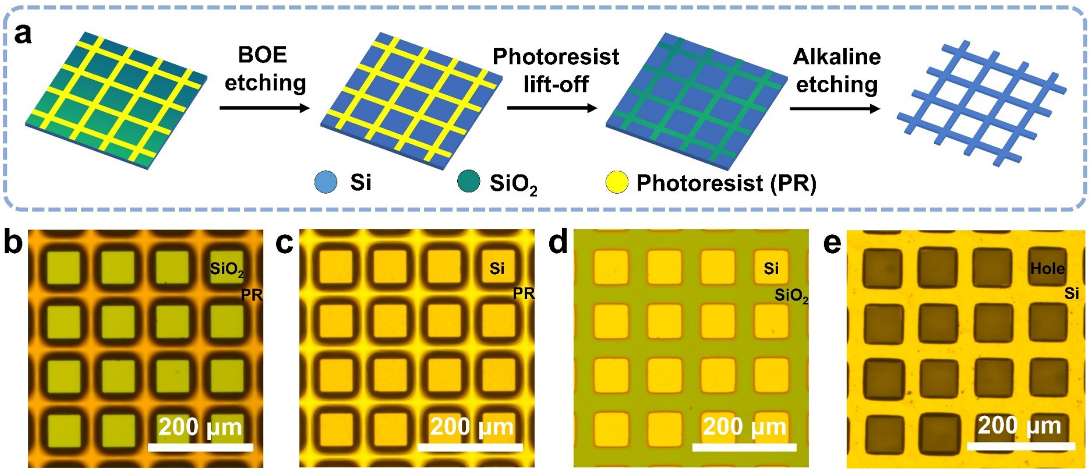

Fig. 2 Alkali etching of the silicon wafer with patterned silica as the mask. (a) Flowchart of the silica-masked alkali etching. Microscopic photographs of the silicon wafer (b) with the photoresist pattern, (c) after the oxide layer at the unmasked region removed, and (d) with the photoresist removed. (e) A microscopic photograph of the obtained single-crystalline silicon frameworks (sc-SiFs).

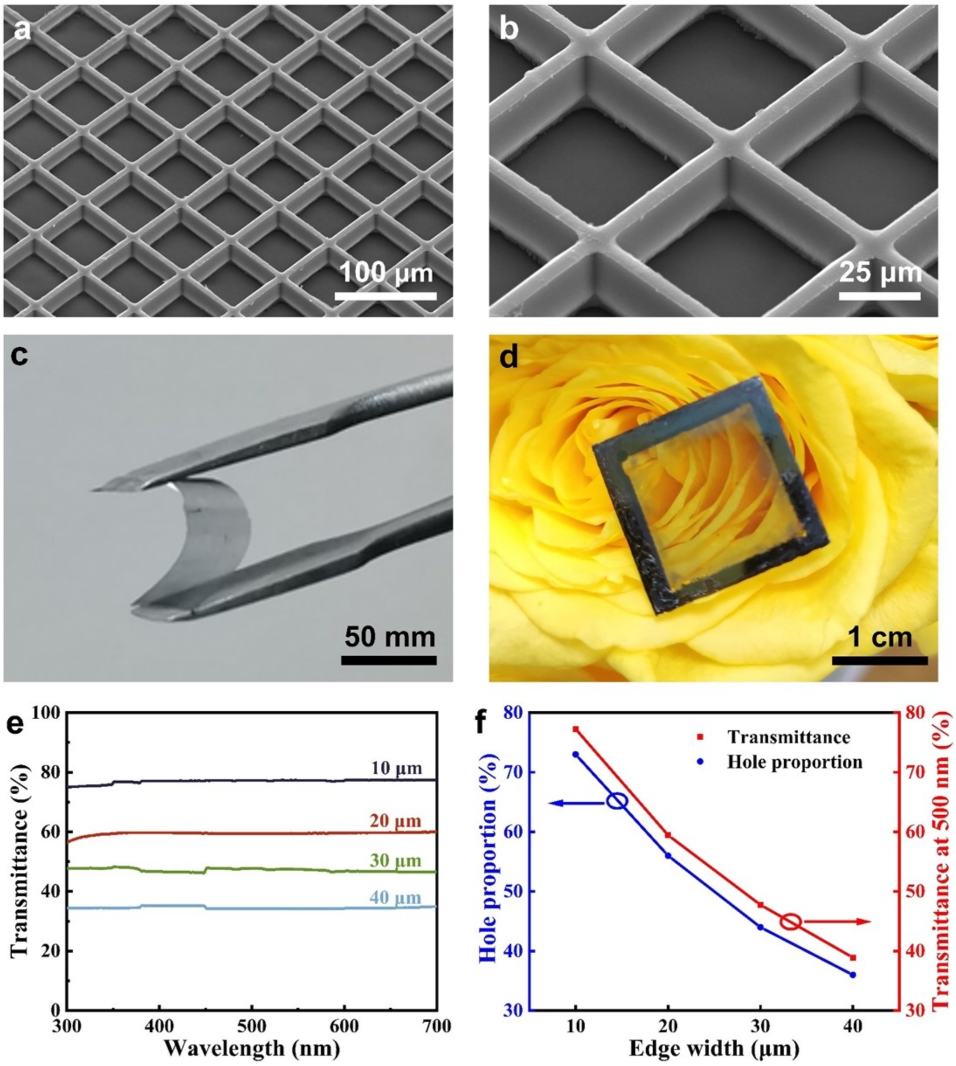

Fig. 3 Characterization of the morphology and properties of sc-SiFs. (a, b) SEM images of sc-SiFs at 45° oblique angle at different magnifications. (c) Optical image of a 20 µm-thick sc-SiFs bent between tweezers and (d) a 20 µm-thick sc-SiFs on rose. (e) Transmittance of sc-SiFs with different edge widths in the visible wavelength range. (f) Transmittance at 500 nm wavelength and hole proportion of sc-SiFs with the same edge length of 60 µm and different edge widths.

they are taken out from the solution due to the action of surface tension. Moreover, they are also fragile during the subsequent process of device fabrication. In our experiments, 20 µm is almost the smallest thickness to ensure the robustness of the sc-SiFs, which was adopted as the sample thickness to balance the property and robustness in this work.

The sc-SiFs were characterized with a scanning electron microscope (SEM). The sample is uniform with periodic grid structures (Fig. 3(a)). A magnified SEM image shows that the surface of the sidewall is smooth without obvious etching damage (Fig. 3(b)). In contrast, the sc-SiFs fabricated by dry etching have relatively high surface roughness (Fig. S3, ESI†).[48] Therefore, sc-SiFs obtained by wet etching are advantageous for photoelectric devices with less surface recombination. The sc-SiFs show good flexibility and transparency. A piece of 20 µm-thickness sc-SiFs can be easily bent with a very small radius of 6 mm (Fig. 3(c)), which indicates that they have potential for devices with mechanical imperceptibility. Moreover, the sc-SiFs can be highly transparent and visually imperceptible (Fig. 3(d)). The transparency of sc-SiFs is related to their structure parameters (Fig. 3(e) and (f)). For samples with a fixed edge length of 60 µm, the transparency increases with the decrease of the edge width. A high transparency of 77 % was obtained in the sample with the edge width of 10 µm. Moreover, the transparency for each sample is slightly higher than the hole proportion due to the incomplete light absorption of sc-SiFs (Fig. 3(f)).[49] The results imply that the transparency of sc-SiFs can be rationally controlled by changing the hole proportion with structure parameters. The minimum edge width is set as 10 µm, and the corresponding transmittance of the sample is 77%. Higher transmittance (i.e. smaller edge width) will lead to increased fabrication complexity, because the edge with

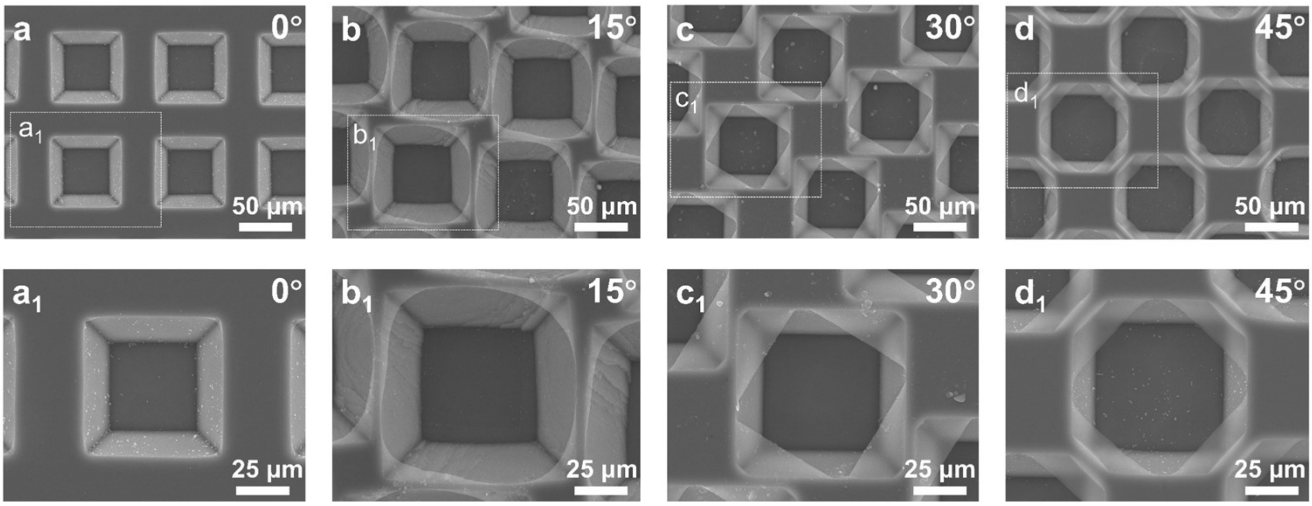

Fig. 4 SEM images of the morphology of sc-SiFs with different lithography directions. (a, a_1) The mask direction is parallel to the silicon wafer orientation. (b, b_1) The angle between mask direction and silicon wafer orientation is 15 °. (c, c_1) The angle between mask direction and silicon wafer orientation is 30 °. (d, d_1) The angle between mask direction and silicon wafer orientation is 45 °.

smaller width is easy to be excessively etched or fracture when they are taken out from the solution due to the action of surface tension.

During the etching process, the crystal orientation of the silicon wafer plays a crucial role in determining the etching morphology. For alkali etching, the etching rates vary with different crystal orientations. The etching rate is fastest along the (110) crystal plane,[50] resulting in preferential etching along this crystal plane. When the edge directions of the photoresist and silica pattern are along <100> crystal orientation on the wafer surface, they are parallel to the (110) crystal plane of the silicon wafer. In this case, the morphology of etched sc-SiFs on the top surface is consistent with the silica pattern. However, because the top surface of the used silicon wafers is (100) crystal plane, it has 45° angles with the sidewalls of the (110) crystal planes (Fig. 4(a_1)). When the edge direction of the photoresist and silica pattern is not parallel to the (100) crystal plane of the silicon wafer, the morphology of etched sc-SiFs deviates from the silica pattern due to the crystallographic selective etching. As the angles between the edge direction of the silica pattern and the <100> crystal orientation of the wafer surface were set as 15°, 30° and 45°, the morphology of sc-SiFs and the silica pattern show similar angles of rotation (Fig. 4). The results provide a new route to finely control the morphology of sc-SiFs by adjusting the pattern angle. Moreover, it is also indicated that the pattern direction should be paid special attention for obtaining sc-SiFs with designed morphology. In order to obtain good alignment, programmatic laser cutting was used to cut the silicon wafer in directions parallel to and perpendicular to the positioning line of the (110) silicon wafer. In the lithography process, the masking pattern is designed with the same square area of 2.0×2.0 cm^2 as the silicon wafers. The masking pattern and the silicon wafers are carefully aligned to match each other.

The potential applications of the flexible and transparent sc-SiFs in mechanically and visually imperceptible electronics were demonstrated through fabricating wearable bending sensors to detect emotion and body action.[40] Sc-SiFs with an edge length of 60 μm and width of 10 μm were chosen as the active materials in account of their high transparency. A 100 μm-thick PDMS layer was used as the substrate and encapsulation layer, and 25 nm-diameter Ag nanowire networks were used as transparent electrodes (Fig. 5(a)). With a total thickness of 200 μm, the sensors can be clamped and transferred with tweezers. With the encapsulation of PDMS, the silver nanowires form a robust conducting network on both ends of the sc-SiFs to ensure reliable electrical contact (Fig. 5(b) and (c)). As a kind of silicon materials, sc-SiFs have piezoresistive effect.[51] The basic response of the relative change of resistance ($\Delta R/R_0$) to deformation was investigated through bending the device at different bending radii and applied different pressures on it (Fig. 5(d)). The electrical current of the device at a constant voltage increased when the device was bent (Fig. 5(e)). The results indicate that the absolute value of the relative change in resistance decreases with the increase of the bending radius and the fitting curve shows an inverse proportional relationship (Fig. 5(f)). When different pressures are applied on the device, the relative change of resistance decreases with the increase of the pressure (Fig. S6, ESI†). The standard curve of the relationship between the relative resistance change and the strain was obtained through calculating the strains corresponding to different bending radii (Fig. 5(g)). The relative change in electrical resistance of the sc-SiFs sensor decreased linearly with the increase of strain. The gauge factor ($GF = \left(\Delta R/R_0\right)/\varepsilon$) represents the sensitivity of the sensor and is calculated as -17 according to the slope of the fitting line. The negative gauge factor is consistent with the piezoresistance effect of n-type silicon.[52] The resolution of the sensor (R)

referred to be minimum strain signal that can be detected and is calculated as 0.02% strain according to Equation (2).

$$R = \sigma/GF \tag{2}$$

where σ is the standard deviation of 0 strain measurement. The stability of the sensor was measured through cyclically testing its response to bending at a 12.5 mm radius for 9 days with 60 cycles per day (Fig. 5(h)). The signals of the sensor kept stable in the total 540 loading and unloading cycles, indicating good stability. With the features of high flexibility and transparency, the sensor can conformally contact with skins without a sense of restraint and is visually inconspicuous (Fig. 5(i)). Three devices were adhered to the skin around the corners of the eyes, the skin near the corner of the mouth, and the neck skin for the detection of blinking, smiling, and swallowing, respectively. It is important to consider the motion artifacts and false signals that can be caused by poor adhesion and conformal contact.[53,54] In our experiments, the skin secretion can help eliminate the air between the device and the skin, enabling the attach of the sensor on the skin under the action of atmospheric pressure. For the applications of emotion and swallow detection, the skin in the attached positions of the face and neck mainly undergoes large-radius bending. Due to the above reasons, the sensor can keep conformally contact with the skin in these applications and effectively detect the emotion and swallow. The devices in Fig. 5(i) were not connected to other electrical wiring and exhibit the concept of transparent devices based on sc-SiFs. In the practical testing process, the two ends of the device were conducted out with elastic silver pastes and two 25 μm-diameter silver wires. Nevertheless, it is believed that all-transparent wearable systems can be realized through integrating with transparent power sources and transparent signal processing and transmission devices. Constant voltages were applied to the devices, and the currents were recorded and transferred to the relative change in resistance. As shown in Fig. 5(j) and (k), the $\Delta R/R_0$ obviously decreased with eye blinking and smiling, and then recovered as the actions stopped. The relative change of resistance can be attributed to the deformation of the skin and the attached devices induced by the actions. Swallow was monitored by the sensor adhered to the throat. In the test, swallow amplitude got stronger with the decrease of saliva when continuously swallowing. As a result, the swallow peak values of $\Delta R/R_0$ gradually decreased (Fig. 5(l)). The results indicate that the imperceptible wearable bending sensors can be effectively applied to detect emotions and tiny motions. It is noted that the detection of blinking, smiling and swallowing is significant for healthcare and communication. For example, the average frequency of human blinking is 12 times per minute. An abnormal increase in blinking frequency may be related to conjunctivitis, xerophthalmia, or attention deficit hyperactivity disorder (ADHD).[55–57] Both blinking and smiling are also forms of human body language and ways of emotional communication. In addition, the monitoring of swallow amplitude can be used to reflect inhaled by mistake, choking water, or airway obstruction of vegetative patients and help save their lives.[58–60]

Conclusions

In conclusion, this study has introduced an innovative strategy for the fabrication of flexible and transparent sc-SiFs by using wet etching, addressing the limitations posed by traditional rigid silicon in wearable electronics. The prepared sc-SiFs exhibit a minimum bending radius of 6 mm and a remarkable light transmittance of up to 77%. By precisely controlling the structural parameters, it is possible to tailor the flexibility and transparency of SiFs to meet the diverse requirements of various applications. Furthermore, the immense potential of the flexible and transparent sc-SiFs in the development of imperceptible wearable electronics was demonstrated by taking the wearable bending sensor as an example. The sensor has been successfully fabricated and implemented to detect facial expressions such as blinking, smiling, and swallowing, which are significant for healthcare, human-machine interaction, and various other fields. This work provides an efficient and scalable method for fabricating flexible and transparent silicon materials, which will provide a new material choice for imperceptible wearable electronics.

Experimental section

Fabrication and characterization of sc-SiFs

Sc-SiFs were fabricated from double-side polished and oxidized, 200 μm thick, 1–10 Ω·cm, n-type, (100)-oriented Si wafers. The Si wafer was cut into 2.0×2.0 cm^2 pieces. A photoresist mask for patterning oxide layer was formed through spin-coating photoresist (AZ 4620), exposure and development processes. Then, the wafers fixed by fixtures with single-side square window were immersed in 40% HF solution for 36 s to fully remove the oxide layer on the side without the photoresist pattern, and a bare Si window (1.5×1.5 cm^2) was obtained. Following that, the wafer was etched in 50% KOH solution at 95 °C for 90 min and the thickness of the wafer was reduced to 65 μm. Next, the sample was released from the fixtures. The side with photoresist pattern was immersed in a BOE buffered etching solution for 4 min to fabricate patterned oxide layer. After that, the sample was etched in 50% KOH solution at 95 °C for 15 min to obtain sc-SiFs. Last, the sc-SiFs underwent multiple cleaning processes, including rinsing, ultrasonic cleaning, and soaking, to reduce excessive residues in experiments. The structures and morphologies of the sc-SiFs were characterized by using SEM (Hitachi, SU5000). The transparency of the sc-SiFs with different structure parameters was measured using ultraviolet-visible spectrophotometer (Hitachi, U-3900).

Fabrication and characterization of wearable sc-SiFs sensors

Wearable sc-SiFs sensors were fabricated on quartz plates cleaned by acetone, deionized water and ethanol, respectively. First, a fluorine-containing hydrophobic solution (DELO) thin layer was spin-coated on the quartz plate to facilitate the final stripping. Second, a polydimethylsiloxane (PDMS, Sylgard 184) layer was spin-coated on the quartz plate at 1000 rpm for 30 s and baked at 100 °C for accelerated curing. After the solidifying

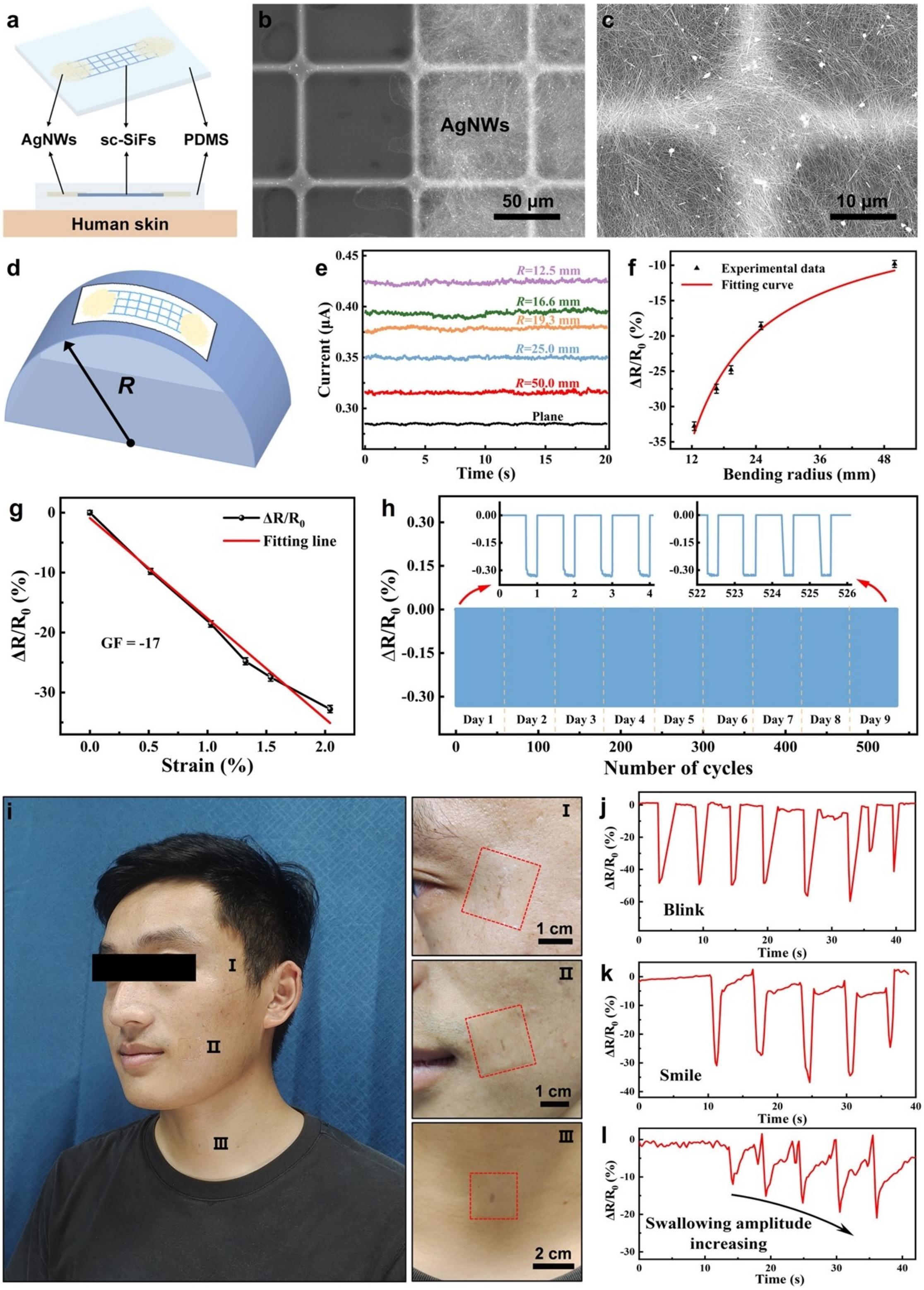

Fig. 5 sc-SiFs-based bending sensors for wearable applications. (a) Schematic of the device structure of the wearable sc-SiFs bending sensor. (b) SEM image of the sc-SiFs bending sensor. (c) SEM image of the silver nanowire electrodes on the sc-SiFs bending sensor. (d) Experimental setup for applying bending strain on the sensor. (e) Electrical current of the device attached on cylinders with different radii. (f) Relationship between the relative change of resistance and the bending radii. (g) The relative change in resistance of the sc-SiFs sensor at different strains. (h) Long-term stability of the bending sensor. (i) Digital photos of the sensors attached to different parts of the human body for sensing various signals. (j) Blinking bending strain sensing data. (k) Smiling bending strain sensing data. (l) Swallowing bending strain sensing data.

of PDMS, the sc-SiFs were placed onto the PDMS substrate. Fluorine-containing hydrophobic solution (DELO) was drop-coated on the intermediate part of the current substrate including the sc-SiFs and dried to form hydrophobic surface. After that, the ethanolic solution of Ag nanowires (25 nm in diameter and 20 μm in length) was spin-coated to form networks suspended on the two ends of the sc-SiFs as transparent electrodes. Eventually, another layer of ultrathin PDMS was spin-coated on the top of the device for encapsulation. The morphology of the silver nanowire electrodes was characterized by using SEM (Hitachi, SU5000). All electrical measurements of the wearable sc-SiFs sensors were performed using a semiconductor electrical test and analysis system (LinkZill, LK-TFT-IV).

Stability testing of the wearable sc-SiFs sensors

One end of the sc-SiFs sensor was attached to the surface of a semi-cylinder with the radius of 12.5 mm, and the other end of the sensor was connected to a mechanical arm keyboard clicker, which drove this end of the sensor to attach and separate from the surface of the semi-cylinder. For each cycle, the sc-SiFs sensor was kept attaching on the surface for 3 s, and then recovered to the unbent state and was kept for 7 s. At the same time, the current under the fixed voltage of 2 V was measured in real time by a source meter (Kelthley 2636B). The test lasted for 9 days with 60 cycles per day.

Note: The experiments involving human subjects were performed with the full consent of the participants.

Conflicts of interest

There are no conflicts of interest to declare.

Acknowledgements

This work was financially supported by the Major International (Regional) Joint Research Project of the National Natural Science Foundation of China (Grant No. 51920105005), the Foundation for Innovation Research Groups of the National Natural Science Foundation of China (Grant No. 51821002), the National Natural Science Foundation of China (No. 52103306), the Open Project of Key Lab of Advanced Optical Manufacturing Technologies of Jiangsu Province (ZZ2308), the Natural Science Foundation of Jiangsu Province (No. BK20210719), the Suzhou Key Laboratory of Functional Nano and Soft Materials, the Collaborative Innovation Center of Suzhou Nano Science and Technology, the Priority Academic Program Development of Jiangsu Higher Education Institutions (PAPD), the 111 Project, and the Joint International Research Laboratory of Carbon-Based Functional Materials and Devices.

References

1 Y. Song, R. Y. Tay, J. Li, C. Xu, J. Min, E. Shirzaei Sani, G. Kim, W. Heng, I. Kim and W. Gao, *Sci. Adv.*, 2023, **9**, eadi6492.

2 D. Franklin, A. Tzavelis, J. Y. Lee, H. U. Chung, J. Trueb, H. Arafa, S. S. Kwak, I. Huang, Y. Liu, M. Rathod, J. Wu, H. Liu, C. Wu, J. A. Pandit, F. S. Ahmad, P. M. McCarthy and J. A. Rogers, *Nat. Biomed. Eng.*, 2023, **7**, 1229–1241.

3 A. F. Azocar, L. M. Mooney, J. F. Duval, A. M. Simon, L. J. Hargrove and E. J. Rouse, *Nat. Biomed. Eng.*, 2020, **4**, 941–953.

4 M. Zhu, Z. Sun, Z. Zhang, Q. Shi, T. He, H. Liu, T. Chen and C. Lee, *Sci. Adv.*, 2020, **6**, eaaz8693.

5 L. Wang, N. Li, Y. Zhang, P. Di, M. Li, M. Lu, K. Liu, Z. Li, J. Ren, L. Zhang and P. Wan, *Matter*, 2022, **5**, 3417–3431.

6 J. Liang, H. Sheng, H. Ma, P. Wang, Q. Wang, J. Yuan, X. Zhang, M. Shao, W. Li, E. Xie, W. Lan, J. Liang, H. Sheng, H. Ma, P. Wang, Q. Wang, J. Yuan, X. Zhang, M. Shao, E. Xie, W. Lan and W. Li, *Adv. Mater. Technol.*, 2023, **8**, 2201234.

7 H. U. Chung, A. Y. Rwei, A. H. Fargette, S. Xu, K. H. Lee, E. C. Dunne, Z. Xie, C. Liu, A. Carlini, D. H. Kim, D. Ryu, E. Kulikova, J. Cao, I. C. Odland, K. B. Fields, B. Hopkins, A. Banks, C. Ogle, D. Grande, J. Bin Park, J. Kim, M. Irie, H. Jang, J. H. Lee, Y. Park, J. Kim, H. H. Jo, H. Hahm, R. Avila, Y. Xu, M. Namkoong, J. W. Kwak, E. Suen, M. A. Paulus, R. J. Kim, B. V. Parsons, K. A. Human, S. S. Kim, M. Patel, W. Reuther, H. S. Kim, S. H. Lee, J. D. Leedle, Y. Yun, S. Rigali, T. Son, I. Jung, H. Arafa, V. R. Soundararajan, A. Ollech, A. Shukla, A. Bradley, M. Schau, C. M. Rand, L. E. Marsillio, Z. L. Harris, Y. Huang, A. Hamvas, A. S. Paller, D. E. W. Mayer, J. Y. Lee and J. A. Rogers, *Nat. Med.*, 2020, **26**, 418–429.

8 W. Wang, Y. Jiang, D. Zhong, Z. Zhang, S. Choudhury, J.-C. Lai, H. Gong, S. Niu, X. Yan, Y. Zheng, C.-C. Shih, R. Ning, Q. Lin, D. Li, Y.-H. Kim, J. Kim, Y.-X. Wang, C. Zhao, C. Xu, X. Ji, Y. Nishio, H. Lyu, J. B. H. Tok and Z. Bao, *Science*, 2023, **380**, 735–742.

9 N. Dai, I. M. Lei, Z. Li, Y. Li, P. Fang and J. Zhong, *Nano Energy*, 2023, **105**, 108041.

10 T. Proietti, C. O'Neill, L. Gerez, T. Cole, S. Mendelowitz, K. Nuckols, C. Hohimer, D. Lin, S. Paganoni and C. Walsh, *Sci. Transl. Med.*, 2023, **15**, eadd1504.

11 D. Won, J. Bang, S. H. Choi, K. R. Pyun, S. Jeong, Y. Lee and S. H. Ko, *Chem. Rev.*, 2023, **123**, 9982–10078.

12 X. Wang, L. Zhi and K. Müllen, *Nano Lett.*, 2008, **8**, 323–327.

13 J. Geng, L. Liu, S. B. Yang, S. C. Youn, D. W. Kim, J. S. Lee, J. K. Choi and H. T. Jung, *J. Phys. Chem. C*, 2010, **114**, 14433–14440.

14 D. R. Sahu, S. Y. Lin and J. L. Huang, *Appl. Surf. Sci.*, 2006, **252**, 7509–7514.

15 G. Brändén, G. Hammarin, R. Harimoorthy, A. Johansson, D. Arnlund, E. Malmerberg, A. Barty, S. Tångefjord, P. Berntsen, D. P. DePonte, C. Seuring, T. A. White, F. Stellato, R. Bean, K. R. Beyerlein, L. M. G. Chavas, H. Fleckenstein, C. Gati, U. Ghoshdastider, L. Gumprecht, D. Oberthür, D. Popp, M. Seibert, T. Tilp, M. Messerschmidt, G. J. Williams, N. D. Loh, H. N. Chapman, P. Zwart, M. Liang, S. Boutet, R. C. Robinson and R. Neutze, *Nat. Commun.*, 2019, **10**, 1–9.

16 P. Won, J. J. Park, T. Lee, I. Ha, S. Han, M. Choi, J. Lee, S. Hong, K. J. Cho and S. H. Ko, *Nano Lett.*, 2019, **19**, 6087–6096.

17 I. Hong, Y. Roh, J. S. Koh, S. Na, T. Kim, E. Lee, H. An, J. Kwon, J. Yeo, S. Hong, K. T. Lee, D. Kang, S. H. Ko and S. Han, *Adv. Mater. Technol.*, 2019, **4**, 1800422.

18 J. Xu, S. Wang, G. J. N. Wang, C. Zhu, S. Luo, L. Jin, X. Gu, S. Chen, V. R. Feig, J. W. F. To, S. Rondeau-Gagné, J. Park, B. C. Schroeder, C. Lu, J. Y. Oh, Y. Wang, Y. H. Kim, H. Yan, R. Sinclair, D. Zhou, G. Xue, B. Murmann, C. Linder, W. Cai, J. B. H. Tok, J. W. Chung and Z. Bao, *Science*, 2017, **355**, 59-64.

19 H. Zhang, Y. Hu, X. Chen, L. Yu, Y. Huang, Z. Wang, S. Wang, Y. Lou, X. Ma, Y. Sun, J. Li, D. Ji, L. Li, W. Hu, H. Q. Zhang, Y. X. Hu, X. S. Chen, L. Yu, Y. N. Huang, Z. W. Wang, S. G. Wang, Y. P. Lou, Y. J. Sun, J. Li, D. Y. Ji, L. Q. Li, X. N. Ma and W. P. Hu, *Adv. Funct. Mater.*, 2022, **32**, 2111705.

20 C. Wei, L. Bai, X. An, M. Xu, W. Liu, W. Zhang, M. Singh, K. Shen, Y. Han, L. Sun, J. Lin, Q. Zhao, Y. Zhang, Y. Yang, M. Yu, Y.

Li, N. Sun, Y. Han, L. Xie, C. Ou, B. Sun, X. Ding, C. Xu, Z. An, R. Chen, H. Ling, W. Li, J. Wang and W. Huang, *Chem*, 2022, **8**, 1427–1441.
21 J. Zhang, X. Song, L. Wang and W. Huang, *Natl. Sci. Rev.*, 2022, **9**, nwab129.
22 Y. Lei, Y. Chen, R. Zhang, Y. Li, Q. Yan, S. Lee, Y. Yu, H. Tsai, W. Choi, K. Wang, Y. Luo, Y. Gu, X. Zheng, C. Wang, C. Wang, H. Hu, Y. Li, B. Qi, M. Lin, Z. Zhang, S. A. Dayeh, M. Pharr, D. P. Fenning, Y. H. Lo, J. Luo, K. Yang, J. Yoo, W. Nie and S. Xu, *Nature*, 2020, **583**, 790–795.
23 J. Huang, Z. Lu, J. He, H. Hu, Q. Liang, K. Liu, Z. Ren, Y. Zhang, H. Yu, Z. Zheng and G. Li, *Energy Environ. Sci.*, 2023, **16**, 1251–1263.
24 H. Lee, S. Hong, J. Lee, Y. D. Suh, J. Kwon, H. Moon, H. Kim, J. Yeo and S. H. Ko, *ACS Appl. Mater. Interfaces*, 2016, **8**, 15449–15458.
25 H. Moon, H. Lee, J. Kwon, Y. D. Suh, D. K. Kim, I. Ha, J. Yeo, S. Hong and S. H. Ko, *Sci. Rep.*, 2017, **7**, 41981.
26 J. Jung, H. Cho, R. Yuksel, D. Kim, H. Lee, J. Kwon, P. Lee, J. Yeo, S. Hong, H. E. Unalan, S. Han and S. H. Ko, *Nanoscale*, 2019, **11**, 20356–20378.
27 H. Lee, H. Kim, I. Ha, J. Jung, P. Won, H. Cho, J. Yeo, S. Hong, S. Han, J. Kwon, K. J. Cho and S. H. Ko, *Soft Robot.*, 2019, **6**, 760–767.
28 P. Won, K. Kyu Kim, H. Kim, J. Jae Park, I. Ha, J. Shin, J. Jung, H. Cho, J. Kwon, H. Lee, S. Hwan Ko, P. Won, K. K. Kim, H. Kim, J. J. Park, I. Ha, J. Shin, J. Jung, H. Cho, S. H. Ko, J. Kwon and H. Lee, *Adv. Mater.*, 2021, **33**, 2002397.
29 S. Hong, H. Lee, J. Lee, J. Kwon, S. Han, Y. D. Suh, H. Cho, J. Shin, J. Yeo, S. Hwan Ko, S. Hong, H. Lee, J. Lee, J. Kwon, S. Han, Y. D. Suh, H. Cho, J. Shin, S. H. Ko and J. Yeo, *Adv. Mater.*, 2015, **27**, 4744–4751.
30 S. Han, J. Kim, Y. Lee, J. Bang, C. G. Kim, J. Choi, J. Min, I. Ha, Y. Yoon, C. H. Yun, M. Cruz, B. J. Wiley and S. H. Ko, *Nano Lett.*, 2022, **22**, 524–532.
31 S. Jeong, H. Cho, S. Han, P. Won, H. Lee, S. Hong, J. Yeo, J. Kwon and S. H. Ko, *Nano Lett.*, 2017, **17**, 4339–4346.
32 G. Gao, F. Yang, F. Zhou, J. He, W. Lu, P. Xiao, H. Yan, C. Pan, T. Chen, Z. Lin Wang, G. Gao, W. Lu, P. Xiao, H. Yan, T. Chen, J. He, C. Pan, Z. L. Wang, F. Yang and F. Zhou, *Adv. Mater.*, 2020, **32**, 2004290.
33 J. W. Kim, J. M. Myoung, J. W. Kim and J. M. Myoung, *Adv. Funct. Mater.*, 2019, **29**, 1808911.
34 T. Shi, X. Chen, R. He, H. Huang, X. Yuan, Z. Zhang, J. Wang, P. K. Chu and X. F. Yu, *Adv. Sci.*, 2023, **10**, 2302005.
35 B. Saruhan, R. Lontio Fomekong and S. Nahirniak, *Front. Sens.*, 2021, **2**, 657931.
36 Z. Q. Zheng, J. D. Yao, B. Wang and G. W. Yang, *Sci. Rep.*, 2015, **5**, 1–8.
37 S. Huang, Y. Liu, Y. Zhao, Z. Ren and C. F. Guo, *Adv. Funct. Mater.*, 2019, **29**, 1805924.
38 T. Wang, K. Lu, Z. Xu, Z. Lin, H. Ning, T. Qiu, Z. Yang, H. Zheng, R. Yao and J. Peng, *Crystals*, 2021, **11**, 511.
39 R. Feiner and T. Dvir, *Nat. Rev. Mater.*, 2017, **3**, 17076.
40 M. Ge, C. Cao, G. M. Biesold, C. D. Sewell, S.-M. Hao, J. Huang, W. Zhang, Y. Lai, Z. Lin, M. Ge, C. Cao, W. Zhang, G. M. Biesold, C. D. Sewell, S. Hao, Z. Lin, J. Huang and Y. Lai, *Adv. Mater.*, 2021, **33**, 2004577.
41 B. Zhang, Y. Shi, J. Mao, S. Huang, Z. Shao, C. Zheng, J. Jie and X. Zhang, *Adv. Mater.*, 2021, **33**, 2008171.
42 J. Park, K. Lee and K. Seo, *Cell Rep. Phys. Sci.*, 2022, **3**, 100715.
43 K. Lee, N. Kim, K. Kim, H.-D. Um, W. Jin, D. Choi, J. Park, K. J. Park, S. Lee and K. Seo, *Joule*, 2020, **4**, 235–246.
44 K. Lee, J. Park and K. Seo, *Small*, 2023, **19**, 2301480.
45 W. Liu, Y. Liu, Z. Yang, C. Xu, X. Li, S. Huang, J. Shi, J. Du, A. Han, Y. Yang, G. Xu, J. Yu, J. Ling, J. Peng, L. Yu, B. Ding, Y. Gao, K. Jiang, Z. Li, Y. Yang, Z. Li, S. Lan, H. Fu, B. Fan, Y. Fu, W. He, F. Li, X. Song, Y. Zhou, Q. Shi, G. Wang, L. Guo, J. Kang, X. Yang, D. Li, Z. Wang, J. Li, S. Thoroddsen, R. Cai, F. Wei, G. Xing, Y. Xie, X. Liu, L. Zhang, F. Meng, Z. Di and Z. Liu, *Nature*, 2023, **617**, 717–723.
46 S. Tian, J. Sun, S. Yang, P. He, G. Wang, Z. Di, G. Ding, X. Xie and M. Jiang, *Sci. Rep.*, 2016, **6**, 34127.
47 H. Seidel, L. Csepregi, A. Heuberger and H. Baumgärtel, *J. Electrochem. Soc.*, 1990, **137**, 3612–3626.
48 C. D. W. Wilkinson and M. Rahman, *Philos. Trans. R. Soc. A Math. Phys. Eng. Sci.*, 2004, **362**, 125–138.
49 G. Li, H. Li, J. Y. L. Ho, M. Wong and H. S. Kwok, *Nano Lett.*, 2014, **14**, 2563–2568.
50 I. Zubel, *J. Micromech. Microeng.*, 2019, **29**, 093002.
51 A. A. Barlian, W. T. Park, J. R. Mallon, A. J. Rastegar and B. L. Pruitt, *Proc. IEEE*, 2009, **97**, 513–552.
52 J. S. Milne, A. C. H. Rowe, S. Arscott and Ch. Renner, *Phys. Rev. Lett.*, 2010, **105**, 226802.
53 Z. Jiang, N. Chen, Z. Yi, J. Zhong, F. Zhang, S. Ji, R. Liao, Y. Wang, H. Li, Z. Liu, Y. Wang, T. Yokota, X. Liu, K. Fukuda, X. Chen and T. Someya, *Nat. Electron.*, 2022, **5**, 784–793.
54 L. Che, X. Hu, H. Xu, Y. Liu, C. Lv, Z. Kang, M. Wu, R. Wen, H. Wu, J. Cui, K. Li, G. Qi, Y. Luo, X. Ma, F. Sun, M. Li and J. Liu, *Small*, 2023, 2308312.
55 N. Kim, J. Chen, W. Wang, M. Moradnia, S. Pouladi, M. Kwon, J. Kim, X. Li and J. Ryou, *Adv. Funct. Mater*, 2021, **31**, 2008242.
56 Y. Groen, N. A. Börger, J. Koerts, J. Thome and O. Tucha, *J. Neural Transm.*, 2017, **124**, 27–38.
57 A. Magliacano, M. Rosenfelder, N. Hieber, A. Bender, A. Estraneo and L. Trojano, *Sci. Rep.*, 2021, **11**, 22393.
58 J. Y. Ko, H. Kim, J. Jang, J. C. Lee and J. S. Ryu, *Sci. Rep.*, 2021, **11**, 5795.
59 R. Shahmoon, Y. Tamir, Y. Beiderman, S. Agdarov, Y. Beiderman and Z. Zalevsky, *Sci. Rep.*, 2022, **12**, 3847.
60 T. Nishino, *Front. Physiol.*, 2013, **3**, 489.